Banner appropriate to article type will appear here in typeset article

Surface corrugations induce helical near-surface flows and transport in microfluidic channels

- Christina Kurzthaler^{1,2,3}, Danielle L. Chase^{1,3}, and Howard A. Stone ¹†
- ¹Department of Mechanical and Aerospace Engineering, Princeton University, New Jersey 08544, USA
- ²Max Planck Institute for the Physics of Complex Systems, 01187 Dresden, Germany
- ³C. K. and D. L. C. contributed equally.
- 7 (Received xx; revised xx; accepted xx)
- We study theoretically and experimentally pressure-driven flow between a flat wall and a
- parallel corrugated wall, a design widely used in microfluidics for low-Reynolds-number 9
- mixing and particle separation. In contrast to previous work, which focuses on recirculating 10
- helicoidal flows along the microfluidic channel that result due to its confining lateral walls, we 11
- study the three-dimensional pressure and flow fields and trajectories of tracer particles at the 12
- scale of each corrugation. Employing a perturbation approach for small surface roughness, 13
- we find that anisotropic pressure gradients generated by the surface corrugations, which are 14
- tilted with respect to the applied pressure gradient, drive transverse flows. We experimentally 15
- measure the flow fields using particle image velocimetry and quantify the effect of the ratio
- of the surface wavelength to the channel height on the transverse flows. Further, we track 17
- tracer particles moving nearby the surface structures and observe three-dimensional skewed 18
- helical trajectories. Projecting the helical motion to two dimensions reveals oscillatory near-19 surface motion with an overall drift along the surface corrugations, reminiscent of earlier 20
- experimental observations and independent of the secondary helical flows that are induced 2.1
- by confining lateral walls. Finally, we quantify the hydrodynamically-induced drift transverse 22
- to the mean flow direction as a function of distance to the surface and the wavelength of the 23
- surface corrugations. 24

Key words:

25

1. Introduction 26

- The development of microfluidic devices has lead to novel technological and biomedical 27
- applications by making possible rapid sorting, mixing, and focusing of various small 28
- biological or synthetic constituents (Giddings 1993; Stone et al. 2004; Whitesides 2006; 29
- Shields IV et al. 2015). The future design of 'lab-on-a-chip' devices, which, due to their 30
- small size, can be routinely used in different settings, could be important for, e.g., the 31
- analysis of single-cells (Stott et al. 2010; Hosic et al. 2016; Qasaimeh et al. 2017; Farahinia 32
 - † Email address for correspondence: hastone@princeton.edu

 et al. 2021), thereby, allowing for rapid disease detection or for advancing the fundamental understanding of biological processes.

Microfluidic approaches have been utilized to guide and control transport processes for several objectives. Examples range from the separation of the components of blood, such as red or white blood cells (Huang *et al.* 2004; Davis *et al.* 2006; McGrath *et al.* 2014), to the focusing and detection of biological cells (Qasaimeh *et al.* 2017; Farahinia *et al.* 2021), to the mixing of particulate suspensions (Stroock *et al.* 2002*b,a*; Stroock & McGraw 2004). The underlying methods rely on different physical mechanisms, such as 'active' concepts, which use externally applied forces and filters (Giddings 1993; Stone *et al.* 2004; Shields IV *et al.* 2015), or 'passive' concepts, which exploit hydrodynamic effects due to fluid inertia (Segré & Silberberg 1961; Di Carlo *et al.* 2007; Humphry *et al.* 2010), pillar arrays in channels (Huang *et al.* 2004; Davis *et al.* 2006; McGrath *et al.* 2014), or patterned microfluidic walls (Stroock *et al.* 2002*b*; Asmolov *et al.* 2015; Choi & Park 2007; Hsu *et al.* 2008; Choi *et al.* 2011; Qasaimeh *et al.* 2017).

Several passive approaches utilize surface topography, relying on the careful design and synthesis of surface structures, mostly, at the micron scale. Corrugations oriented obliquely to the axial flow direction or v-shaped herringbone structures were originally proposed for the mixing of laminar streams (Stroock et al. 2002a,b; Stroock & McGraw 2004). In addition to mixing, passive approaches have been used to separate or detect particles. For example, microfluidic channels with oblique corrugations on one wall have been applied widely to separate colloidal particles (Choi & Park 2007; Hsu et al. 2008; Choi et al. 2011) and for the detection of plasma (Qasaimeh et al. 2017) or circulating tumor cells (Stott et al. 2010). The parallel oblique corrugations on the top or bottom wall generate a transverse pressure gradient and, due to the lateral confinement of the channel, helical streamlines result, where the pitch of the helix spans several corrugations (Stroock et al. 2002a,b; Stroock & McGraw 2004). The recirculating flows generated by the corrugations, which will be in opposite lateral directions at the corrugated and flat surfaces, transport particles to each lateral wall depending on the particle's position along the channel height, which depends, for example on the particle's size or density, and can be controlled using inertial focusing (Segré & Silberberg 1961; Di Carlo et al. 2007). Therefore, particles with different properties can be transported to opposite lateral walls and sorted according to the property of interest. Similarly, v-shaped, or herringbone, corrugations create counter-rotating vortices in the microchannel. These flows bring particles to their equilibrium configuration between adjacent vortices either near the herringbone surface or near the planar wall, depending on their density, to separate particles into different streams for sorting or detection (Hsu et al. 2008).

The aforementioned studies focused on the recirculating flows, generated by surface topography, at the scale of the channel size. The effect of surface structure on the flow and particle motion nearby the surface, at the scale of individual corrugations, remains relatively unexplored. Recent insights for the non-trivial trajectories come from our work on particle sedimentation nearby corrugated surfaces (Chase *et al.* 2022), where we quantified, experimentally and theoretically, the impact of corrugation shape and particle size on the transport behavior without background flow and due only to the disturbance flow generated by the interaction of the particle and surface structure. In contrast to results observed in microfluidic channels, where particles are separated by size due to differences in their equilibrium position along the channel height, it was shown that the magnitude of the lateral displacement for particles of different sizes depends not only on their distance to the corrugated wall, but on non-trivial relationships between the particle size and corrugation wavelength.

Here, we complement these findings by studying pressure-driven flow between a corrugated surface and a parallel flat wall. Using a perturbation ansatz for the amplitude of the

83 surface structure, we calculate the pressure field induced by the surface pattern and derive analytical expressions for the three-dimensional flow fields up to the second order in the 84 surface roughness. Based on these results, we determine the motion of tracer particles near 85 the corrugated wall. While the large-scale helicoidal flows in corrugated microchannels, 86 generated by the combined effect of the corrugations and the lateral confining walls, have a 87 diameter equal to that of the channel dimension and a pitch of several wavelengths (Stroock 88 89 et al. 2002a), our results reveal that tracer particles also follow three-dimensional helical trajectories, independent of the lateral confining walls, which have a pitch of one wavelength 90 and a diameter that depends on the distance to the corrugated surface and the corrugation 91 wavelength. Projected to two dimensions, the trajectories of tracer particles resemble the 92 oscillatory near-surface motion observed in several experiments (Choi & Park 2007; Hsu 93 94 et al. 2008; Choi et al. 2011; Qasaimeh et al. 2017). The oscillatory pattern is characterized by near-surface particle motion along the corrugations while moving above grooves and 95 across the corrugations while moving over ridges. Moreover, our results demonstrate that 96 near-surface particles exhibit an overall drift along the surface corrugations, leading to a 97 skewed helical trajectory. We quantify the overall displacement as a function of surface 98 wavelength and particle position along the channel height, showing that the lateral drift can 99 be achieved independent of the recirculating flows generated in closed channels. 100

Our paper is structured as follows: In Section 2, we outline a hydrodynamic model for the pressure-driven flow between a flat wall and a parallel rough wall. In Section 3, we describe our experimental method for measuring the flow field in a corrugated microchannel using particle image velocimetry. To our knowledge, this is the first experimental measurement of velocity fields in corrugated microchannels. We also outline our method for three-dimensional single-particle tracking in the corrugated channels. In Section 4, we provide experimental and theoretical results for the roughness-induced pressure and flow fields and compare them qualitatively and quantitatively. Furthermore, we find good agreement between our experimentally measured mean velocities and the theory from Stroock *et al.* (2002*a*) for flows generated in corrugated microchannels with confining lateral walls. Most importantly, our results are complemented by theoretical and experimental measurements of three-dimensional helical particle trajectories. Finally, we investigate the effect of the ratio of corrugation wavelength to channel height for varying positions along the channel height on the lateral drift of tracer particles in the flow.

2. Hydrodynamic model

101

102

104

105

106

107

108

109

110

111

112

113

114

115

We consider three-dimensional, low-Reynolds-number, pressure-driven flow between two plates, where the lower surface has a given shape, $z = \epsilon LH(x, y)$, with shape function H(x, y), as indicated in Fig. 1. Here, L denotes the distance between the upper surface and the reference surface S_0 , and we denote by ϵ a dimensionless roughness parameter. The velocity and pressure fields, u(x, y, z) and p(x, y, z), respectively, obey the Stokes and continuity equations,

$$\mu \nabla^2 \boldsymbol{u} = \boldsymbol{\nabla} p \quad \text{and} \quad \boldsymbol{\nabla} \cdot \boldsymbol{u} = 0, \tag{2.1}$$

where μ denotes the fluid viscosity. We have no-slip boundary conditions on the lower and upper surfaces: $u(x, y, z = \epsilon LH(x, y)) = \mathbf{0}$ and $u(x, y, z = L) = \mathbf{0}$. Subsequently, we consider small surface corrugations, corresponding to $\epsilon \ll 1$, and expand the flow field up to third order in the small parameter ϵ ,

$$u = u^{(0)} + \epsilon u^{(1)} + \epsilon^2 u^{(2)} + O(\epsilon^3). \tag{2.2}$$

An average pressure gradient is applied along the direction of the flow, $\langle dp/dx \rangle = -G$,

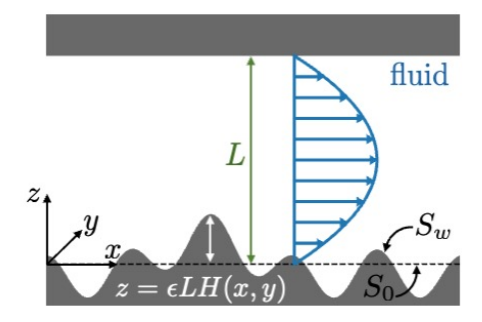


Figure 1: Sketch of pressure-driven flow between the lower corrugated surface S_w and the upper planar wall (side view). Here, L denotes the distance between the upper surface and a reference surface S_0 at z = 0, H(x, y) is the shape function, and ϵ is the surface roughness.

and hence we rescale by

132
$$u = \frac{GL^2}{2\mu}U$$
, $p = GLP$, $z = LZ$, $x = LX$, $y = LY$. (2.3)

By using the method of domain perturbation (Kamrin *et al.* 2010; Kurzthaler *et al.* 2020), we obtain the boundary conditions for the components of the expansion:

136
$$U^{(0)} = \mathbf{0}, \quad U^{(1)} = -H(X,Y) \frac{\partial U^{(0)}}{\partial Z} \Big|_{Z=0},$$
137
$$U^{(2)} = -H(X,Y) \frac{\partial U^{(1)}}{\partial Z} \Big|_{Z=0} - \frac{1}{2} H(X,Y)^2 \frac{\partial^2 U^{(0)}}{\partial Z^2} \Big|_{Z=0} \quad \text{on } Z = 0, \qquad (2.4a)$$
138
$$U^{(0)} = \mathbf{0}, \quad U^{(1)} = \mathbf{0}, \quad U^{(2)} = \mathbf{0} \quad \text{on } Z = 1. \qquad (2.4b)$$

We note that the zeroth-order flow field is pressure-driven flow between parallel plates, $U^{(0)} = Z(1-Z)e_X$ and the pressure is $P^{(0)} = -Xe_X$. Thus, the boundary conditions (2.4a) on Z=0 simplify to: $U^{(1)}(X,Y,Z=0)=-H(X,Y)e_X$ and $U^{(2)}(X,Y,Z=0)=-H(X,Y)\partial U^{(1)}/\partial Z|_{Z=0}+H(X,Y)^2e_X$.

Generally, one can calculate the first-order perturbation $U^{(1)}$ by applying a Fourier transform to the X- and Y-components,

146
₁₄₇

$$\tilde{U}(K_X, K_Y, Z) = \frac{1}{2\pi} \int_{\mathbb{R}^2} e^{-i(K_X X + K_Y Y)} U(X, Y, Z) \, dX dY; \tag{2.5}$$

the inverse transform is $U(X,Y,Z) = (2\pi)^{-1} \int_{\mathbb{R}^2} e^{\mathrm{i}(K_X X + K_Y Y)} \tilde{U}(K_X,K_Y,Z) \, \mathrm{d}K_X \mathrm{d}K_Y$. The Stokes and continuity equations (2.1) then simplify to

$$\left(\frac{\mathrm{d}^2}{\mathrm{d}Z^2} - K^2\right)\tilde{\boldsymbol{U}}^{(1)} = \left(\mathrm{i}\boldsymbol{K} + \boldsymbol{e}_Z \frac{\mathrm{d}}{\mathrm{d}Z}\right)\tilde{P}^{(1)},\tag{2.6a}$$

$$i\mathbf{K} \cdot \tilde{\mathbf{U}}^{(1)} + \frac{d\tilde{W}^{(1)}}{dZ} = 0, \tag{2.6b}$$

where we have used $\tilde{\boldsymbol{U}}^{(1)} = [\tilde{U}^{(1)}, \tilde{V}^{(1)}, \tilde{W}^{(1)}]^T$, $\boldsymbol{K} = [K_X, K_Y, 0]^T$, and $K = |\boldsymbol{K}|$. Rearranging (2.6*a*)-(2.6*b*) provides an equation for the pressure field,

$$\left(\frac{\mathrm{d}^2}{\mathrm{d}Z^2} - K^2\right)\tilde{P}^{(1)} = 0,\tag{2.7}$$

which can be solved by $\tilde{P}^{(1)} = p_0(K) \exp(-KZ) + p_1(K) \exp(KZ)$. Using this form as input for Eqs. (2.6a)-(2.6b), we can calculate the velocity field $U^{(1)}$ and determine the coefficients p_0 and p_1 by enforcing the boundary conditions [Eqs. (2.4a)-(2.4b)], which depend on the surface shape H(X,Y). Knowledge of the first-order flow field $U^{(1)}$ then allows us to iteratively compute the second-order flow field $U^{(2)}$ with boundary conditions in Eqs. (2.4a)-(2.4b). The velocity fields obtained via the domain-perturbation approach have been validated with numerical simulations of the full hydrodynamic flows (assuming a shear-flow scenario) by Roggeveen et al. (2023). In particular, the error of the perturbative approach remained small for small surface roughness and moderate for large wavelengths $\lambda/L \geq 2$.

It is worth emphasizing that the theory is, in principle, valid for arbitrary surface shapes. However, analytical progress is limited by whether the surface shape function H(X,Y) and powers of it (e.g., $H(X,Y)^2$ is required for the second-order flow field) have an analytically tractable Fourier transform. Furthermore, one may need to perform a numerical backtransform of the pressure and flow fields to real space. For cosine and sine functions, the calculations can be done analytically. Consequently, for every shape function, which can be expanded in terms of a Fourier series (i.e., periodic, piece-wise continuous, and integrable over the period), our approach allows calculating (semi-)analytically the flow fields.

At this point, we want to mention that the stream function for two-dimensional shear flow near a periodic surface has been addressed recently (Assoudi *et al.* 2018). Also, analytical work on the three-dimensional streamlines over sinusoidal surface grooves, tilted with respect to the principal flow direction, has provided a prediction for the helicity of the flow (Stroock *et al.* 2002a). The same authors later calculated the flow over herringbone structures in a channel of finite width in terms of a Fourier expansion by approximating the surface grooves with an effective slip velocity (Stroock & McGraw 2004). The focus of the latter study, however, was on the impact of the corrugated surfaces on the mixing of particulate suspensions.

3. Experimental methods

We fabricate two channels, both with corrugations of wavelength λ on the top wall, but with different channel heights L, therefore varying the ratio of λ/L . We 3D print molds of the negative of each channel (Formlabs Form 2) and cast a clear channel from polydimethylsiloxane (PDMS). We punch inlet and outlet holes and bond the PDMS channel to a glass slide (Fig. 2a). One channel has a height $L=320~\mu m$ and surface amplitude $\epsilon L=30~\mu m$. The second channel has a height $L=615~\mu m$ and surface amplitude $\epsilon L=60~\mu m$. The wavelength of the surface corrugations for both channels is $\lambda=600~\mu m$, and the aspect ratio (width to height) of both channels is 10. The channel height and corrugation wavelength and amplitude were measured by filling the channel with a fluorescent dye and taking xz images using a confocal microscope (Leica) (Fig. 2b).

To measure the flow field in the channel, we use a syringe pump, with prescribed flow rates of 2.5 and 10 μ L min⁻¹, respectively, for the L=320 and 615 μ m channels, to flow a suspension of neutrally buoyant fluorescent 1 μ m diameter tracer particles through the channel. We use a confocal microscope (Leica) to image a 916 μ m \times 916 μ m section in xy at a frame rate of 7.4 fps and capture 200 frames. Using PIV Lab (Thielicke & Sonntag 2021; Stamhuis & Thielicke 2014) in MATLAB (MathWorks), we perform particle image velocimetry of the steady flow field to measure the axial and transverse components of the velocity. We image at 40 different z positions along the channel height. A stack of 200 time series images at z=120 μ m is shown in Fig. 2c, where the oscillations of the streamlines are visible as bright streaks.

In addition to measuring the flow field in the xy-plane, we can measure the three-

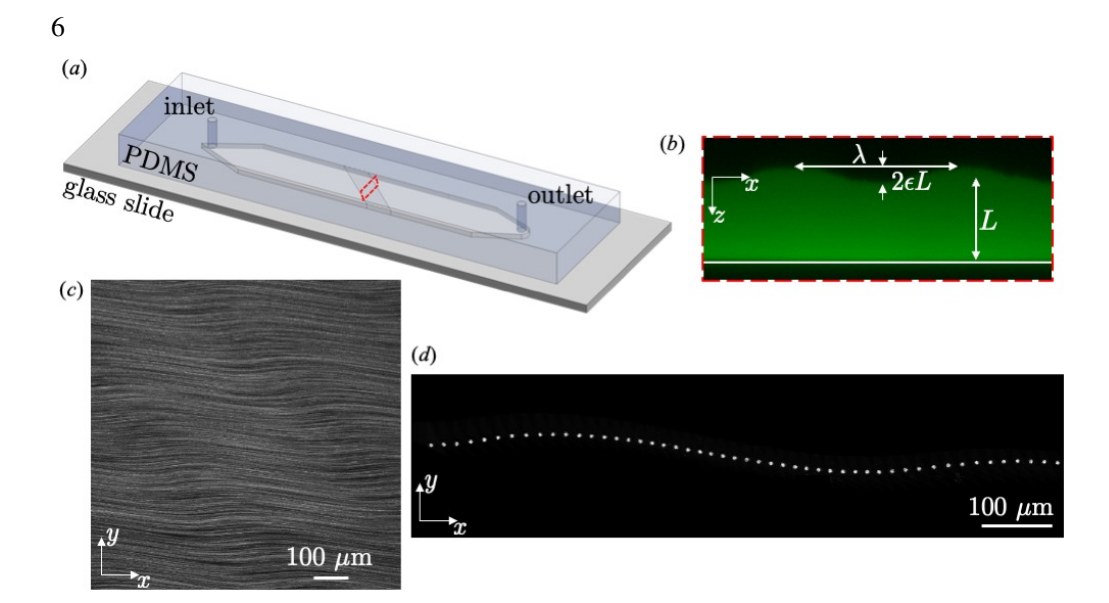


Figure 2: Experiments: (a) The channel used in the experimental system is cast polydimethysiloxane with corrugations on the upper wall. (b) A cross-sectional view of the channel visualized with fluorescent dye. Here, the wavelength is $\lambda = 600~\mu m$, the height is $L = 320~\mu m$, and the amplitude is $\epsilon L = 30~\mu m$. (c) Flow field visualization of pressure-driven flow in the corrugated channel from a time stack of 200 experimental images taken at a frame rate of 7.4 fps with 1 μm diameter fluorescent particles. (d) Visualization of the trajectory of a 5 μm diameter particle in pressure-driven flow in the corrugated channel.

dimensional trajectories of individual tracer particles. For the same channels, we flow a dilute suspension of neutrally buoyant fluorescent tracer particles with a diameter of 5 μ m through the channel at a constant flow rate using a syringe pump. We take xyzt images using a confocal microscope (Leica). The xy image is 916 μ m by 230 μ m, and we image 27 sections in z with a step size of 2.365 μ m at a frame rate of 18 fps, acquiring the xyz volume in 1.5 seconds. For every time step, we find the (x, y) location of the particle using the circle detection algorithm in MATLAB (Mathworks). We determine the z position of the particle at each time step by first cropping the image around the particle location and calculating $G(z) = \sum I(x, y)$, where I(x, y) is the image intensity, for each image in the z-stack. The image with max(G) is determined to be the z position of the particle. We iterate this process for each time step to find the particle trajectory (x(t), y(t), z(t)). A sample trajectory, projected to the xy plane, is shown as the superposition of the frames of the determined best z position for each time step in Fig. 2d.

Our experiments have Stokes number $S_{tk} \approx 10^{-9}$, where the Stokes number is defined by $S_{tk} = \frac{\rho_p d_p^2 U}{18\mu D}$. Here ρ_p is the particle density, d_p is the particle diameter, U is the characteristic fluid velocity, μ is the fluid viscosity, and D is the hydraulic diameter of the channel.

4. Results and discussion

While the theory presented in Section 2 is valid for arbitrary surface shapes, here we study the aspect of parallel corrugations, reminiscent of the widely used pattern in microfluidic devices (Stroock *et al.* 2002*b*; Choi & Park 2007; Hsu *et al.* 2008; Choi *et al.* 2011; Qasaimeh *et al.* 2017). We consider a surface shape $H(X,Y) = \cos(K_0(X+Y))$ characterized by the wavenumber $k_0 = K_0/L$, corresponding to a wavelength $\lambda = 2\pi/k_0$. We note that the surface

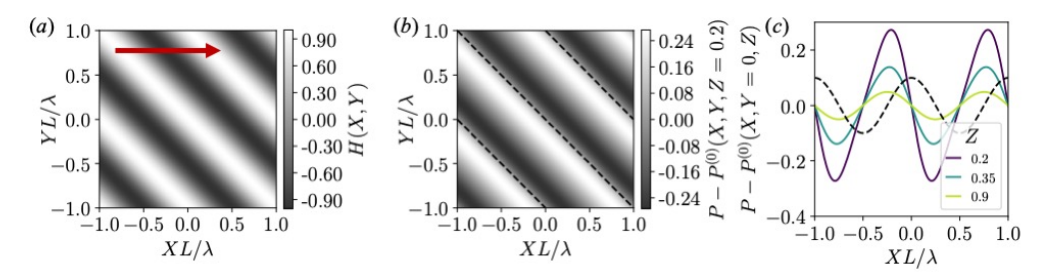


Figure 3: Surface structure and roughness-induced pressure. (a) Contour plot of the surface structure H(X,Y). The gray shaded areas indicate the height profile of the underlying surface, where dark areas correspond to grooves and white areas to ridges, respectively. The arrow indicates the direction of the applied pressure gradient (b) Contour plot of the roughness-induced components of the pressure field $P - P^{(0)} = \epsilon P^{(1)} + \epsilon^2 P^{(2)}$ at the center of the channel Z = 0.2. Here, the black dashed lines correspond to the maxima of the surface structure. (c) Roughness-induced pressure along X at Y = 0 for varying Z. The black dashed line corresponds to H(X,Y). The wavelength in (b) and (c) is $\lambda/L = 2$. The applied pressure gradient is in the X direction.

corrugations are at an angle of $\pi/4$ to the direction of the applied pressure gradient (see Fig. 3a). In what follows, we refer to fluid transport along corrugations when a fluid particle moves on a path in the positive *X*-direction but with displacement in the negative *Y*-direction, and across corrugations when the flow path is instead in the positive *Y*-direction.

To compute the pressure and flow fields, we follow the general approach outlined in Section 2. Therefore, we use the Fourier transform of the surface shape $\tilde{H}(K_X, K_Y) = \pi[\delta(K_0 + K_X)\delta(K_0 + K_Y) + \delta(K_0 - K_X)\delta(K_0 - K_Y)]$, where $\delta(\cdot)$ denotes the delta function, as input to calculate the pressure $\tilde{P}^{(1)}$ and the velocity field $\tilde{U}^{(1)}$ in Fourier space and transform it back to real space analytically. We repeat this for the second-order flow field $U^{(2)}$, where the Fourier backtransform is still doable but becomes tedious. An alternative way to compute the flow fields, which relies on the sinusoidal form of the surface shape, is outlined by Roggeveen *et al.* (2023).

4.1. Roughness-induced pressure fields

We find that the surface corrugations lead to the generation of a pressure field P that varies with position. In particular, the zeroth-order pressure field is $P^{(0)} = -X$ and the first-order pressure field evaluates to

$$P^{(1)}(X,Y,Z) = \sin(K_0(X+Y)) \frac{K_0 e^{-K_0\sqrt{2}(2+Z)}}{(1+4K_0^2 - \cosh(2\sqrt{2}K_0))} \times \left[e^{2\sqrt{2}K_0Z} + e^{4\sqrt{2}K_0} + \left(2\sqrt{2}K_0 - 1\right) e^{2\sqrt{2}K_0(Z+1)} - e^{2\sqrt{2}K_0} \left(2\sqrt{2}K_0 + 1\right) \right].$$
246
$$(4.1)$$

Higher-order terms are lengthy and not presented here. For a corrugated surface $H(X,Y) = \cos(K_0(X+Y))$ (see Fig. 3a), the roughness-induced contributions to the pressure field at Z=0.2 are shown in Fig. 3b. Plotting the roughness-induced contributions to P along X at Y=0 for varying Z-positions (Fig. 3c), we see that the pressure builds up in front of the surface ridges and decreases in front of the surface grooves, where the surface shape is depicted by the black dashed line.

In particular, the first-order contribution to the pressure, which can be abbreviated by $P^{(1)} = \sin(K_0(X+Y))\bar{P}^{(1)}(Z)$ [Eq. (4.1)], has its extrema at the inflection points of the surface, i.e., at points of vanishing curvature, $\cos(K_0(X+Y)) = 0$. The extrema are at



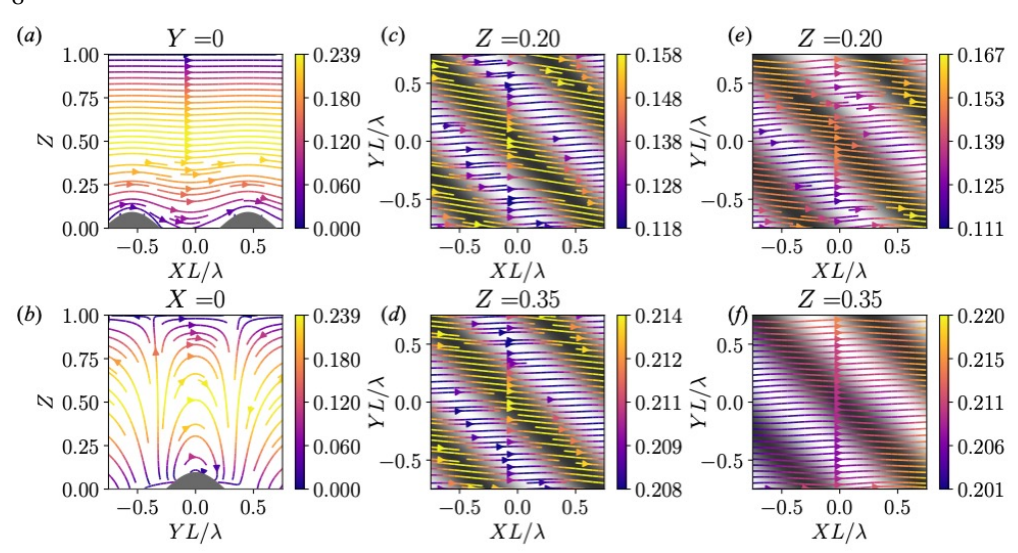


Figure 4: Theoretical and experimental velocity fields. (a) Streamlines of the theoretical velocity field in the XZ- plane, $[U^{(0)} + \epsilon U^{(1)} + \epsilon^2 U^{(2)}, W^{(0)} + \epsilon W^{(1)} + \epsilon^2 W^{(2)}]^T$ and (b) YZ- plane, $[V^{(0)} + \epsilon V^{(1)} + \epsilon^2 V^{(2)}, W^{(0)} + \epsilon W^{(1)} + \epsilon^2 W^{(2)}]^T$. The gray areas indicate the surface shape from the side. (c-d) Streamlines of the theoretical velocity field in the XY-plane, $[U^{(0)} + \epsilon U^{(1)} + \epsilon^2 U^{(2)}, V^{(0)} + \epsilon V^{(1)} + \epsilon^2 V^{(2)}]^T$, at (c) Z = 0.20 and (d) Z = 0.35. The gray shaded areas indicate the height profile of the underlying surface, where dark areas correspond to grooves and white areas to ridges, respectively (see colormap in Fig. 3(a)). (e-f) Streamlines of the experimental velocity field in the XY-plane at (c) Z = 0.20 and (d) Z = 0.35. In all panels the wavelength is $\lambda/L = 1.87$ and the surface roughness is $\epsilon = 0.094$. Furthermore, the color map corresponds to the magnitude of the velocity in a particular plane. Note that for the experimental velocities, the magnitude includes only the X and Y components of the velocity, since the Z component is not measured.

 $X+Y=(2n+1)\pi/(2K_0)=(2n+1)\lambda/(4L)$ for $n \in \mathbb{Z}$, with minima at $X+Y=(4n+1)\lambda/(4L)$ and maxima at $X+Y=(4n-1)\lambda/(4L)$. The inflection points are modified by the second-order contribution $P^{(2)}$.

We find that the magnitude of the roughness-induced contributions to the pressure decrease as Z increases, moving towards the flat upper wall (Fig. 3). Finally, we note that the pressure field generated by the corrugated surface is anisotropic relative to the direction of the applied pressure gradient, along X, (Fig. 3b) and can therefore induce, in addition to flows along the Z-direction, transverse flows (in the XY-plane).

4.2. Roughness-induced flow fields

The streamlines along the channel (XZ-plane), shown in Fig. 4a, display oscillations over the surface corrugations, which vanish near the flat upper wall. Furthermore, we find a non-vanishing lateral velocity field in the YZ-plane (Fig. 4b), which is solely generated by the corrugated surface. In particular, the flow moves in opposite Y-directions over surface ridges compared to grooves. This response leads to flow patterns, which alternate their direction depending on the underlying surface structure.

The streamlines (XY-plane) are oscillatory in the transverse direction (Y-direction), transporting fluid along the direction of the corrugations above surface grooves and across the corrugations above ridges; see Fig. 4c-d for Z=0.20 and Z=0.35, respectively. The gray shaded background depicts the height of the underlying surface with height map corresponding to Fig. 3a. The oscillations are a result of the pressure field and, consequently,

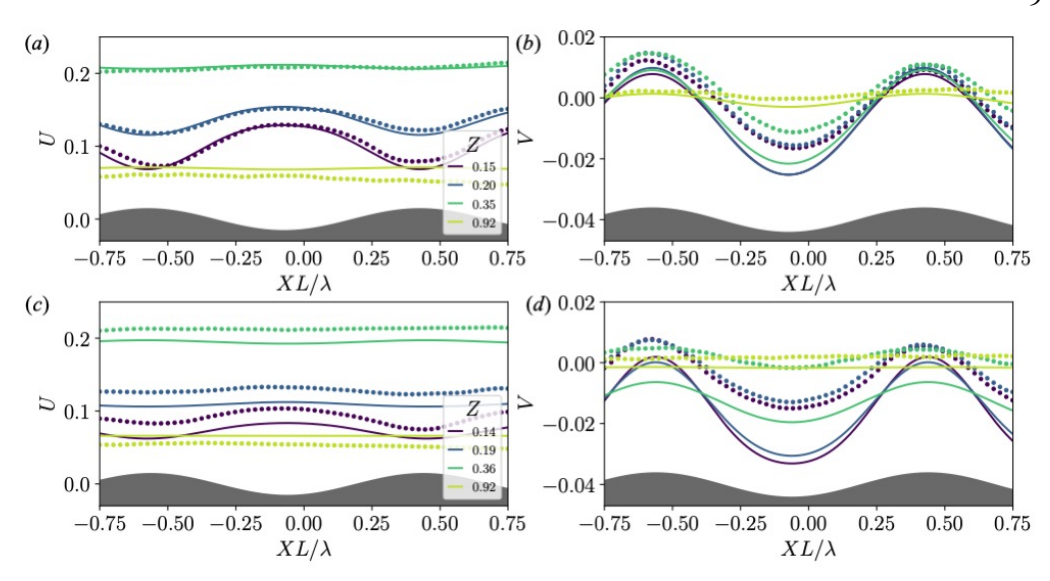


Figure 5: Theoretical and experimental velocities for varying λ/L . The measured experimental and theoretical X and Y velocities, U and V, along Y = 0 for $(a-b) \lambda/L = 1.87$ and $(c-d) \lambda/L = 0.98$ for varying Z positions. The symbols indicate the experimental data and the solid lines are the theoretical prediction. The gray areas indicate the surface shape at the position along X.

the pressure gradients generated due to the corrugated surface structure (Fig. 3b-c). The pressure gradient over the grooves has $\frac{dP}{dY} > 0$, which generates flow along the corrugations, in the negative Y-direction. Flow moves across the corrugations (positive Y-direction) over the ridges, where $\frac{dP}{dY} < 0$. As expected, the oscillatory flow becomes weaker for increasing Z. We also observe that, nearby the surface, the flow along the surface grooves is faster than above the surface ridges. To compare our experimental measurements to theoretical predictions, we rescale the experimental measurements using (2.3), where G is determined for pressure-driven flow in a rectangular channel with prescribed flow rate Q and channel height and width L and w, respectively. Therefore, $G = \frac{12\mu Q}{wL^3} \left(1 - \frac{6L}{w} \sum_{n=0}^{\infty} \Lambda_n^{-5} \tanh\left(\Lambda_n \frac{w}{L}\right)\right)^{-1}$, with

 $\Lambda_n = \frac{(2n+1)\pi}{2}$. Comparing experimental results with the theoretical predictions (Fig. 4c-d), we find qualitatively similar behavior, where fluid is transported along the grooves and across the ridges. Additionally, both theory and experiments show that the magnitude of the velocity is larger over the grooves than over the ridges. However, the magnitude of the velocity differences, $|U_{\text{groove}} - U_{\text{ridge}}|$ and $|V_{\text{groove}} - V_{\text{ridge}}|$, of our experimental measurements are smaller than the theory predicts; in particular, for Z=0.35 (Fig. 4f), we see very little variation in the velocity between the ridges and the grooves. We believe that the discrepancy between theory and experiments is twofold. While small spatial fluctuations in the velocity field result from the fabrication of our corrugated channels, the overall difference in velocity differences, $|U_{\text{groove}} - U_{\text{ridge}}|$ and $|V_{\text{groove}} - V_{\text{ridge}}|$, results from the absence of channel sidewalls in our theory. We consider this aspect later in more detail and show that the average velocities are better described by the theory of Stroock *et al.* (2002*b*), which accounts for the side walls of the channel (Fig. 6).

We quantitatively compare the theoretical and experimental U and V velocities along X at Y=0 for varying Z positions for pressure-driven flow over a surface with $\lambda/L=1.87$ (Fig. 5a-b). As expected, both the experimental measurements (symbols) and theoretical predictions (solid lines) show that the magnitude of the velocity differences, for both U and

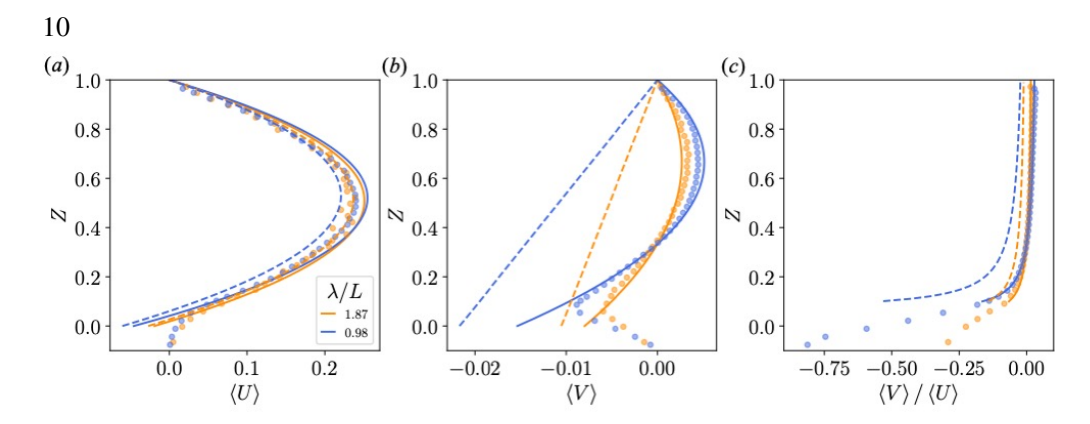


Figure 6: Mean velocities along the channel height for varying λ/L (a) $\langle U \rangle$ and (b) $\langle V \rangle$ averaged over 1.5λ in the X- and Y-directions for various Z positions in the channel. (c) The ratio of $\langle V \rangle/\langle U \rangle$ is an approximation for the drift of a particle in the transverse direction. Large negative values near the corrugated surface indicate drift along the direction of the corrugations. Experimental data are indicated by the symbols. The dotted lines indicate the theory presented in this work for pressure-driven flow between two parallel plates. The solid lines are the theory from Stroock et al. (2002a) for a channel with confining lateral walls (Eqs. A 1a-A 1b).

V, is largest for Z-positions closest to the corrugated surface. Furthermore, we find that the axial velocity U is slower over the surface ridges and faster over the surface grooves. The magnitude of the velocity differences is larger for the transverse velocity V than for the axial velocity U for both the experimental measurements and theoretical predictions. We find that above the surface ridges, the transverse velocity V is positive, leading to transport across the corrugations (in the positive Y-direction), while in the grooves, the velocity is negative, inducing transport along the corrugations (in the negative Y-direction). Furthermore, the magnitude of the transverse velocity V is larger over the grooves than the ridges, for the Z-positions shown here.

In general, we find that the discrepancy between the experimental measurements of the axial velocity compared to the theoretical predictions is larger for the $\lambda/L=0.98$ surface than for the $\lambda/L=1.87$ surface (Fig. 5c-d). In this short wavelength regime, it has been shown numerically that the domain perturbation method for calculating the flow velocities becomes less accurate (Roggeveen *et al.* 2023). Thus, including higher-orders in our small-roughness expansion could capture the experimental observations better. We note that the theoretical prediction of the axial velocity for Z=0.36 is slower above the grooves and faster above the ridges which is the opposite of the theoretical prediction at Z=0.36 for the $\lambda/L=1.87$ surface. We also find that for the transverse velocity V, the experimental measurements are more positive than the theoretical predictions. In fact, the theoretical predictions for V are almost entirely negative, along the surface corrugations. We also find, both experimentally and theoretically, that the axial velocity differences are larger for $\lambda/L=1.87$ than for $\lambda/L=0.98$, and the transverse velocity differences are smaller for $\lambda/L=1.87$ than for $\lambda/L=0.98$. This finding illustrates that there is a nontrivial relationship between the surface structure and the magnitude of the roughness-induced velocities.

In addition to not satisfying $\lambda/L > 1$ for the short wavelength surface $\lambda/L = 0.98$, some of the error between the theoretical model and experimental measurements shown in Figs. 4-5 can be understood by considering the difference in geometry between the theory presented in this work and our experiments. The theory presented here considers pressure-driven flow between two parallel plates, without side walls, while the experiment is a channel that has confining lateral walls. The implication of this difference is that the model allows for a net flux in the transverse direction, while in the experiment, the net flux must be zero in the transverse

direction. The lateral confining walls induce a helicoidal flow, where fluid is transported in the negative Y-direction near the corrugated wall and in the positive Y-direction near the upper flat wall, as described by Stroock et al. (2002a).

333

334

335

336

337

338 339

340

341

342

343

344

345

346

347

348

349

350

351

352

353

354

355

356

357

358

359

360

361

362

363

364

365

367

369

371

379

381

To understand the effects of lateral confining walls, we measure the mean velocities, $\langle U \rangle$ and $\langle V \rangle$ over 1.5 λ in the X- and Y-directions for varying Z and compare our experimental measurements to the theory presented in this work with no lateral walls and to the theory of Stroock et al. (2002a), which includes effects of lateral walls. Fig. 6a shows that our experimental measurements (symbols) agree reasonably well with both the model of Stroock et al. (2002a) (solid lines) and the model presented in this work (dashed lines). Additionally, we are able to experimentally measure the $\langle U \rangle$ velocity for Z < 0, and we do not observe any recirculating flow within the corrugations, which would be indicated by $\langle U \rangle < 0$. The mean transverse velocities are shown in Fig. 6b. Without confining lateral walls, the theory presented here (dashed lines) shows that the mean transverse velocity will always transport fluid along the direction of the corrugations, $\langle V \rangle < 0$, and becomes larger in magnitude close to the corrugations. The confining lateral walls impose the constraint that the net flux in the transverse direction is zero, requiring that, near the upper wall, the mean transverse velocity $\langle V \rangle > 0$. There is a turning point in the lower half of the channel where $\langle V \rangle < 0$. We find good agreement between the model from Stroock et al. (2002a) and our experimental measurements, which indicates that although we do not satisfy $\lambda/L > 1$, the theory still captures the behavior well for $\lambda/L = 0.98$. We note that inside of the corrugations, $Z \leq 0.1$, the experimental measurements of $|\langle V \rangle|$ decrease because they are averaged over the entire cross-section, where a portion is the solid corrugated surface.

Taking $\langle V \rangle / \langle U \rangle$, we obtain the ratio of the net flux in the transverse direction compared to the axial direction, or the direction of the applied pressure gradient. In particular, $\langle V \rangle / \langle U \rangle =$ -1 indicates that the flow direction is parallel to the grooves, at an angle $\pi/4$. We find that, nearby the corrugations and for a given Z, the ratio of $\langle V \rangle / \langle U \rangle$ is more negative for $\lambda/L = 0.98$ than $\lambda/L = 1.87$, indicating that shorter wavelengths produce a larger flux in the transverse direction. This observation is found for both the theory presented in this work and that of Stroock et al. (2002a) and for the experimental measurements. We note that this observation is for tracer particles. For larger particles ($\lambda/a = O(1)$), Chase et al. (2022) shows that transverse displacement depends non-trivially on the interaction between the particle size and surface corrugation wavelength.

4.3. Helical motion of neutrally buoyant tracer particles

We plot the experimental three-dimensional trajectories of tracer particles for $\lambda/L = 1.87$ 366 and 0.98 in Fig. 7a. The three-dimensional motion is helical, where the pitch of the helix is the wavelength of the corrugated surface. This helical trajectory is distinct from the helical 368 streamlines described by Stroock et al. (2002a,b), where the pitch of the helix spans several wavelengths and the diameter is the width of the channel. The mechanism for both of these 370 helical trajectories is due to the corrugated surface, however, the helix we measure is due to the changes in pressure over one wavelength, while the helix measured by Stroock et al. 372 (2002a,b) is due to the confining lateral walls driving flow along the corrugations near the 373 corrugated wall and in the opposite direction near the flat upper wall. Stroock et al. (2002a,b) 374 375 emphasize that the helicoidal flow field is useful for mixing in low-Reynolds-number flows in channels. The smaller scale helical trajectories that we observe nearby the corrugated surface 376 are independent of the background helicoidal flow and could have implications for mixing 377 nearby a contaminated rough surface or transporting the species perpendicular to the rough 378 wall. Furthermore, this mixing occurs independent of the confining lateral channel walls, 380 and, therefore, is generic to flow over rough surfaces in any geometry.

Projecting the three-dimensional helical motion to the XY-plane, as shown in Fig. 7b, we

383

384

385 386

387

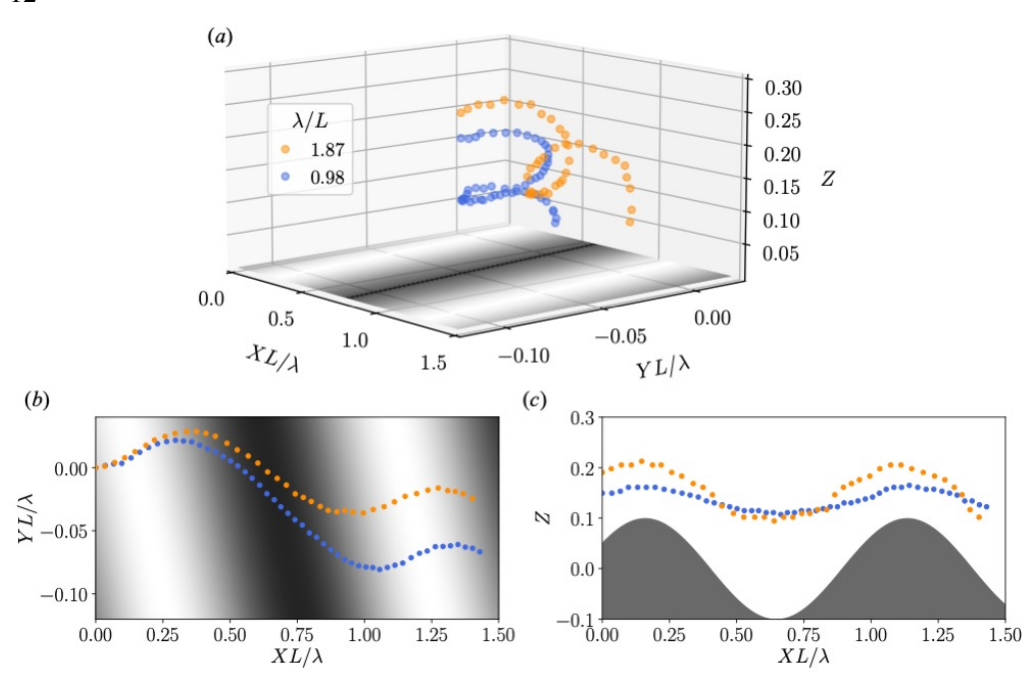


Figure 7: Three-dimensional experimental helical trajectories of tracer particles. (a) Three-dimensional particle trajectories over 1.5λ for $\lambda/L=1.87$ and 0.98 (see experimental methods in Sec. 3). (b) Projection of the three-dimensional trajectories to the XY-plane. (b) Projection of the three-dimensional trajectories to the XZ-plane.

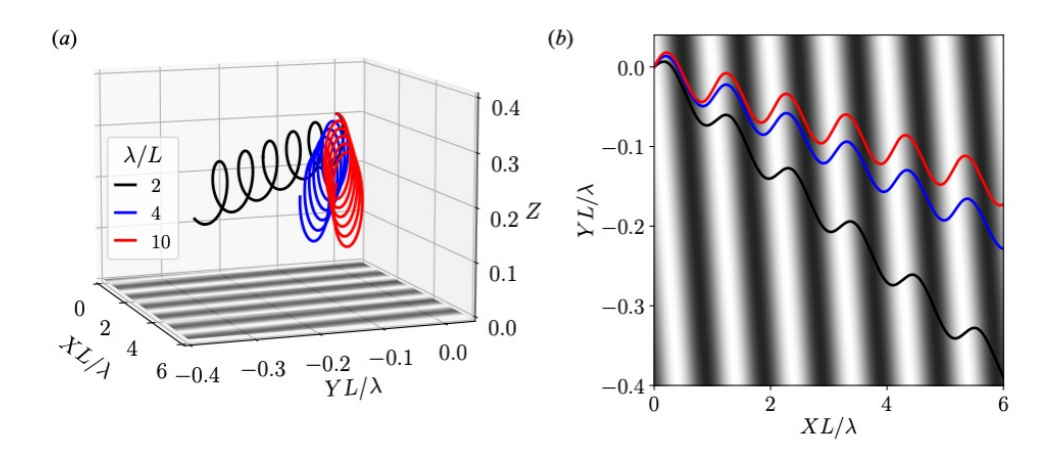


Figure 8: Three-dimensional theoretical helical trajectories of neutrally buoyant point-particles. (a) Three-dimensional particle trajectories over 6λ for $\lambda/L=2,4$, and 10. (b) Projection of of the three-dimensional trajectories to the XY-plane. Z(0)=0.3 for all trajectories.

see that the lateral displacement is larger for the smaller λ/L surface. In addition to the twodimensional measurements that we reported earlier, here we have experimental measurements of the particle's trajectory in the Z-direction (Fig. 7c). We find that the oscillations in the Z-direction are larger for the longer wavelength surface, $\lambda/L=1.87$, despite the smaller lateral displacement.

Our theoretical model allows us to further explore the full ramifications of the three-

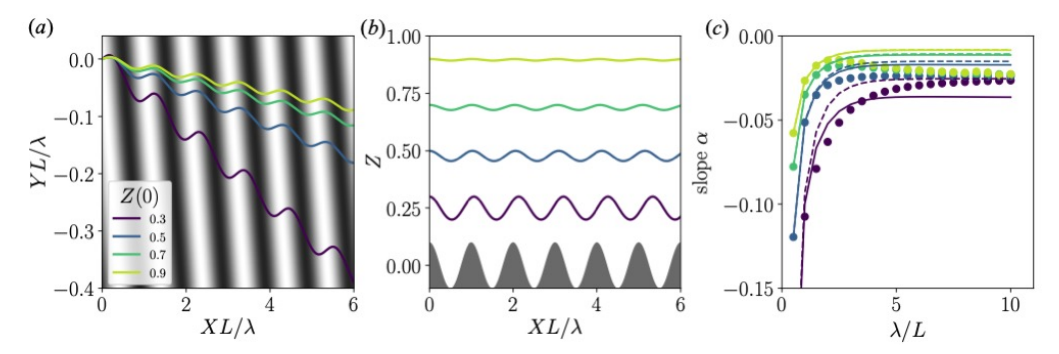


Figure 9: Trajectories of tracer particles near corrugated surfaces. (a-b) Particle trajectories in the (a) XY-plane and (b) XZ- plane for a surface with wavelength $\lambda/L=2$ and roughness $\epsilon=0.1$ and different initial particle-surface distances Z(0). The gray shaded areas in (a) indicate the height of the underlying surface (see colormap in Fig. 3(a)). Gray areas in (b) indicate the surface from the side. (c) Slope of the particle drift in the XY-plane as a function of wavelength λ/L and for different initial particle-surface distances Z(0). The symbols indicate the slopes of the trajectories starting at (X=0,Y=0,Z=Z(0)). The dotted lines correspond to the theoretical prediction of the slope (Eq. (4.3)) by using Z=Z(0) and the solid lines are the predictions using the average distance $\langle Z \rangle$ as input for Eq. (4.3).

dimensional flow and the potential effect of mixing due to the corrugations. We explore the effect of wavelength on the trajectories of tracer particles following the streamlines in pressure-driven flow in a channel with one corrugated surface and one planar surface, without confining lateral walls.

We denote by $\mathbf{r}(t) = [x(t), y(t), z(t)]^T$ the position of a particle at time t. Rescaling length scales by L, time scales by L/U, and velocities by $GL^2/2\mu$, the equation of motion (neglecting hydrodynamic interactions, i.e., point-like particles) obeys:

$$\frac{\mathrm{d}\mathbf{R}}{\mathrm{d}T} = Z(1-Z)\mathbf{e}_X + \epsilon \mathbf{U}^{(1)}(\mathbf{R}) + \epsilon^2 \mathbf{U}^{(2)}(\mathbf{R}),\tag{4.2}$$

where capital letters represent the rescaled variables. For a pressure-driven flow between two planar walls (corresponding to $U^{(1)} = U^{(2)} = 0$) the particle displacements are $\Delta X(T) = TZ(0)(1 - Z(0))$ and $\Delta Y(T) = \Delta Z(T) = 0$, where Z(0) denotes the initial position at time T = 0. The particle trajectory near a corrugated wall is obtained by numerically evaluating Eq. (4.2).

In Fig 8a, we show helical trajectories for $\lambda/L=2$, 4, and 10 starting at a position Z(0)=0.3. We find that the theoretical predictions agree qualitatively with our experimental measurements in that the shortest wavelength surfaces produce the largest drift (Fig. 8b), while having the smallest changes in Z (Fig. 8a). Quantitative comparison between experimental and theoretical three-dimensional trajectories will be influenced by the confining lateral walls in our experiments. Additionally, to compare the net drift of our experimental three-dimensional trajectories with the theoretical predictions, longer experimental trajectories will provide more robust measurements of the net drift, which we leave to future work.

4.4. Hydrodynamically-induced drift

Most importantly, we find that the particle trajectories are oscillatory and display an overall hydrodynamically-induced drift along the surface corrugations. To quantify this behavior further, we have performed simulations for various initial positions Z(0) and wavelengths λ/L and extracted the slope α of the trajectories, see Fig. 9. Our results indicate that the slope of the trajectories, irrespective of Z(0) or λ/L , is negative, and hence, the particles have a

net displacement along the surface grooves. This qualitative behavior is in agreement with experiments of colloidal particles nearby surface corrugations, e.g., Choi & Park (2007); Hsu et al. (2008); Choi et al. (2011). The magnitude of the slope becomes smaller for increasing wavelength λ/L and particle-surface distance Z(0) (Fig. 9c). We further approximate the slope α of the trajectories by integrating the velocities U and V over one wavelength and taking the ratio:

423
$$\alpha \simeq \frac{\int_0^{\lambda/L} V(X, Y, Z) dX}{\int_0^{\lambda/L} U(X, Y, Z) dX} = \frac{\epsilon^2 (1 - Z) \bar{V}_0^{(2)}}{Z(1 - Z) + \epsilon^2 (1 - Z) \bar{U}_0^{(2)}},$$
 (4.3)

where $\bar{U}_0^{(2)}$ and $\bar{V}_0^{(2)}$ are constants. The slope α depends on the dimensionless wavenumber K_0 , the roughness ϵ , and the vertical coordinate Z. We find that the displacement is largest nearby the corrugations and that the effect is strongest for short wavelength surfaces. For long wavelength surfaces, the transport in the simulated trajectories becomes independent of the Z-position. The prediction for the slope α with Z = Z(0) explains fairly well the drift of particles for small λ/L obtained from our simulations, however, it deviates from the data for larger λ/L (Fig. 9c). We note that the vertical motion of the particle varies along its trajectory, which affects the overall drift (Fig. 9b). Therefore, we replace Z by its distance $\langle Z \rangle$ averaged over the surface wavelength λ/L in Eq. (4.3), which allows for a better description of the slope α .

Finally, we again stress that the presented theory is valid for channels of infinite width, so that we do not observe circulating flows in our theoretical results (Stroock *et al.* 2002*a,b*; Stroock & McGraw 2004). In channels with lateral side walls, the experimental near-surface helical flows reported in this work are in addition to the circulating flows along the channel length. In our experiments, we estimate that the pitch of the helix of the channel-scale helicoidal flow is ≈ 20 cm, or $\approx 300\lambda$, compared to the pitch of the near-surface helical flows, $\lambda = 600 \ \mu m$ (see Appendix A).

5. Conclusions

We have shown, theoretically and experimentally, that low-Reynolds-number pressure-driven flow between a flat wall and a parallel corrugated wall, whose corrugations are tilted with respect to the applied pressure gradient, leads to three-dimensional helical streamlines nearby the corrugated surface. Using a perturbation approach for small surface amplitude, our results reveal that, on the scale of each corrugation, the pressure gradients generated by the surface corrugations drive transverse flows generating the helical streamlines. These near-surface flows are in addition to the helicoidal recirculating flows previously studied that are generated by the lateral confining walls of microfluidic channels (Stroock *et al.* 2002*a,b*; Stroock & McGraw 2004).

We find that the roughness-induced pressure builds up approaching a surface ridge and drops in front of a surface groove. These oscillations in the pressure field induce an oscillatory velocity along the flow direction which is faster above the surface grooves than the surface ridges. The velocity in the transverse direction is directed across the ridges and along the grooves and is largest nearby the surface. We find good qualitative agreement between our theory focusing on the scale of one corrugation and our experimental velocity measurements obtained by particle image velocimetry. Furthermore, we find good quantitative agreement between the mean velocities measured in our experiments and those reported by Stroock *et al.* (2002*a*), which account for confining lateral walls. Both our theory and the theory

of Stroock *et al.* (2002*a*) find that short wavelength surfaces induce larger transverse flows nearby the corrugates surface, which our experiments confirm.

By tracking tracer particles moving nearby the surface corrugations, we observe threedimensional skewed helical trajectories, where the particle drifts along the corrugations when close to a groove, while it moves across the corrugations in the presence of a ridge. Overall the particles display a net drift along the surface corrugations, which depends on surface wavelength and particle-surface distance. Our experimental measurements of the helical trajectories show that for longer wavelength surfaces, despite larger oscillations along the channel height, the net drift is smaller than it is for shorter wavelength surfaces. This observation is in agreement with our theoretical predictions.

Our findings rationalize earlier experimental observations on the motion of colloids (Choi & Park 2007; Hsu *et al.* 2008; Choi *et al.* 2011) and biological cells (Qasaimeh *et al.* 2017) nearby corrugated surfaces and demonstrate that particle drift and oscillatory motion can be generated solely by the presence of the corrugated surface, independent of the lateral confining walls. Furthermore, these behaviors appear to be generic across different systems, ranging from pressure driven flows (Choi & Park 2007; Hsu *et al.* 2008; Choi *et al.* 2011; Oasaimeh *et al.* 2017) to particle sedimentation (Chase *et al.* 2022).

The helical flows reported in this work might have implications for near-surface mixing. Their three-dimensional nature also demonstrates that patterned surfaces influence particle motion independent of the helicoidal flows generated due to confining walls (Stroock *et al.* 2002*a,b*; Stroock & McGraw 2004).

Theory and experiments capturing the finite size of the particles are required to fully 481 assess the helical nature of particle trajectories in pressure-driven flow. It may also be 482 interesting to study the effect of different surface shapes, such as, e.g., randomly structured 483 topographies (Charru et al. 2007; Kurzthaler et al. 2020), or particle shapes (Uspal et al. 2013; 484 Georgiev et al. 2020) on the observed flow patterns and trajectories. Understanding these 485 aspects could provide novel ways to manipulate flow and, thereby, particle motion, which 486 could be potentially useful for future technological and biomedical applications involving 487 mixing and sorting. 488

- 489 **Acknowledgements.** We thank Ryan MacElroy for his help designing the microfluidic channels.
- Funding. D.L.C. acknowledges support from the NSF Graduate Research Fellowship Program. H.A.S.
 acknowledges partial support from NSF CBET-2127563.
- 492 **Declaration of interests.** The authors report no conflict of interest.

462

463

464

465

466

467

468

469

470

471

472

473

474

475

476

477

478

479

480

495

493 **Author ORCIDs.** C.K.: 0000-0002-5516-1464; D.L.C.: 0000-0001-6607-7404; H.A.S.: 0000-0002-9670-494 0639

Appendix A. Transverse flows in corrugated channels with side walls

We consider a closed microfluidic channel of width w and height L, which has a corrugated surface topography on the lower channel wall. The surface corrugations are characterized by a wavelength λ and tilted at an angle θ relative to the applied pressure drop. The expressions for the mean axial and transverse velocities in the xy-plane for a thin ($w \gg L$), closed channel with shallow grooves ($\epsilon L \ll L$) (shown in Fig. 6) are from Stroock *et al.* (2002a).

wavelength $\lambda = 600 \, \mu \text{m}$.

521

The mean axial $\langle u \rangle$ and transverse $\langle v \rangle$ velocities are given by

502
$$\langle u \rangle = \frac{6Q}{Lw} \left(1 - \frac{3}{2} \epsilon^2 \left(1 - \tilde{K} \right) \right) \left(\frac{(L-z) \left(z - \tilde{z}_{\text{eff}} \right)}{L^2} \right), \tag{A 1}a)$$

$$\langle v \rangle = \epsilon^2 \frac{6Q}{Lw} \left(\frac{3}{2} \frac{z (L-z)}{L^2} - \frac{L-z}{2L} \right) \left(K_{\parallel} - K_{\perp} \right) \sin \theta \cos \theta, \tag{A 1b}$$

where $\tilde{K} = K_{\perp} \cos^2 \theta + K_{\parallel} \sin^2 \theta$ and $\tilde{z}_{\text{eff}} = z_{\text{eff}\perp} \cos^2 \theta + z_{\text{eff}\parallel} \sin^2 \theta$. The expressions for K_{\parallel} , K_{\perp} , $z_{\text{eff}\parallel}$, and $z_{\text{eff}\perp}$ are

$$K_{\parallel} = -1 + \frac{4\pi L}{\lambda} \left(\frac{\sinh\left(\frac{2\pi L}{\lambda}\right) \cosh\left(\frac{2\pi L}{\lambda}\right) - \frac{2\pi L}{\lambda}}{\sinh\left(\frac{2\pi L}{\lambda}\right)^2 - \left(\frac{2\pi L}{\lambda}\right)^2} \right), \tag{A 2a}$$

$$K_{\perp} = -1 + \frac{2\pi L}{\lambda} \frac{\cosh\left(\frac{2\pi L}{\lambda}\right)}{\sinh\left(\frac{2\pi L}{\lambda}\right)},\tag{A.2b}$$

$$z_{\text{eff}\parallel} = \frac{1}{2} K_{\parallel} L \epsilon^2, \tag{A 2c}$$

$$z_{\text{eff}\perp} = \frac{1}{2} K_{\perp} L \epsilon^2. \tag{A 2d}$$

To compare the near surface helical flows that we measure in this work with the helicoidal flow due to lateral confinement, we compute the expression from Stroock *et al.* (2002*a*),

$$\tan \Omega = \frac{\epsilon^2 (K_{\parallel} - K_{\perp}) \cos \theta \sin \theta}{1 - \epsilon^2 (3/2 - \tilde{K})},$$
 (A 3)

where Ω is the angle between the axial direction of the flow and the direction of flow just below the flat top of the channel. The pitch of the helix is then defined as

$$p = \frac{w}{\tan \Omega}.\tag{A4}$$

The pitch of the helix of the channel-scale helicoidal flow is ≈ 20 cm for our channels of widths w = 320 and 615 μ m, which is three orders of magnitude larger than the scale of the near-surface helical flows reported here, which have a pitch on the scale of the surface

REFERENCES

- ASMOLOV, E. S., DUBOV, A. L., NIZKAYA, T. V., KUEHNE, A. J. C. & VINOGRADOVA, O. I. 2015 Principles of
 transverse flow fractionation of microparticles in superhydrophobic channels. *Lab Chip* 15, 2835–
 2841.
- 525 ASSOUDI, R., LAMZOUD, K. & CHAOUI, M. 2018 Influence of the wall roughness on a linear shear flow. *FME* 526 *Trans.* **46** (2), 272–277.
- 527 Charru, F., Larrieu, E., Dupont, J.-B. & Zenit, R. 2007 Motion of a particle near a rough wall in a viscous 528 shear flow. *J. Fluid Mech.* **570**, 431–453.
- 529 Chase, D. L., Kurzthaler, C. & Stone, H. A. 2022 Hydrodynamically induced helical particle drift due 530 to patterned surfaces. *Proceedings of the National Academy of Sciences* **119** (31), e2202082119.
- Сної, S., Ku, T., Song, S., Choї, C. & Park, J.-K. 2011 Hydrophoretic high-throughput selection of platelets
 in physiological shear-stress range. *Lab Chip* 11, 413–418.
- CHOI, S. & PARK, J.-K. 2007 Continuous hydrophoretic separation and sizing of microparticles using slanted
 obstacles in a microchannel. *Lab Chip* 7, 890–897.

- DAVIS, J. A., INGLIS, D. W., MORTON, K. J., LAWRENCE, D. A., HUANG, L. R., CHOU, S. Y., STURM, J. C.
 & AUSTIN, R. H. 2006 Deterministic hydrodynamics: Taking blood apart. *Proc. Natl. Acad. Sci.* 103 (40), 14779–14784.
- DI CARLO, D., IRIMIA, D., TOMPKINS, R. G. & TONER, M. 2007 Continuous inertial focusing, ordering, and separation of particles in microchannels. *Proc. Natl. Acad. Sci. U.S.A.* **104** (48), 18892–18897.
- FARAHINIA, A., ZHANG, W.J. & BADEA, I. 2021 Novel microfluidic approaches to circulating tumor cell separation and sorting of blood cells: A review. *J. Sci.-Adv. Mater. Dev.* **6** (3), 303–320.
- Georgiev, R. N., Toscano, S. O., Uspal, W. E., Bet, B., Samin, S., van Roij, R. & Eral, H. B. 2020
 Universal motion of mirror-symmetric microparticles in confined Stokes flow. *Proc. Natl. Acad. Sci. U.S.A* 117 (36), 21865–21872.
- 545 GIDDINGS, J. C. 1993 Field-flow fractionation: analysis of macromolecular, colloidal, and particulate materials. *Science* **260** (5113), 1456–1465.
- Hosic, S., Murthy, S. K. & Koppes, A. N. 2016 Microfluidic sample preparation for single cell analysis.
 Anal. Chem. 88 (1), 354–380.
- HSU, C.-H., DI CARLO, D., CHEN, C., IRIMIA, D. & TONER, M. 2008 Microvortex for focusing, guiding and sorting of particles. *Lab Chip* **8**, 2128–2134.
- Huang, L. R., Cox, E. C., Austin, R. H. & Sturm, J. C. 2004 Continuous particle separation through deterministic lateral displacement. *Science* **304** (5673), 987–990.
- Humphry, K. J., Kulkarni, P. M., Weitz, D. A., Morris, J. F. & Stone, H. A. 2010 Axial and lateral particle ordering in finite reynolds number channel flows. *Phys. Fluids* **22** (8), 081703.
- KAMRIN, K., BAZANT, M. Z. & STONE, H. A. 2010 Effective slip boundary conditions for arbitrary periodic surfaces: The surface mobility tensor. *J. Fluid Mech.* **658**, 409–437.
- Kurzthaler, C., Zhu, L., Pahlavan, A. A. & Stone, H. A. 2020 Particle motion nearby rough surfaces.
 Phys. Rev. Fluids 5, 082101.
- McGrath, J., Jimenez, M. & Bridle, H. 2014 Deterministic lateral displacement for particle separation: a
 review. Lab Chip 14 (21), 4139–4158.
- QASAIMEH, M. A., WU, Y. C., BOSE, S., MENACHERY, A., TALLURI, S., GONZALEZ, G., FULCINITI, M., KARP,
 J. M., PRABHALA, R. H. & KARNIK, R. 2017 Isolation of circulating plasma cells in multiple myeloma
 using cd138 antibody-based capture in a microfluidic device. Sci. Rep. 7 (1), 1–10.
- ROGGEVEEN, JV, STONE, HA & KURZTHALER, C 2023 Transport of a passive scalar in wide channels with surface topography: An asymptotic theory. *J. Phys. Condens. Matter* **35** (27), 274003.
- Segré, G. & Silberberg, A. 1961 Radial particle displacements in Poiseuille flow of suspensions. *Nature* 189 (4760), 209–210.
- SHIELDS IV, C.W., REYES, C. D. & LÓPEZ, G. P. 2015 Microfluidic cell sorting: a review of the advances in the separation of cells from debulking to rare cell isolation. *Lab Chip* **15**, 1230–1249.
- 570 Stamhuis, Eize & Thielicke, William 2014 Pivlab–towards user-friendly, affordable and accurate digital particle image velocimetry in matlab. *Journal of open research software* **2** (1), 30.
- 572 Stone, H. A., Stroock, A. D. & Ajdari, A. 2004 Engineering flows in small devices: Microfluidics toward a lab-on-a-chip. *Annu. Rev. Fluid Mech.* **36** (1), 381–411.
- STOTT, S. L., Hsu, C.-H., Tsukrov, D. I., Yu, M., Miyamoto, D. T., Waltman, B. A., Rothenberg, S. M.,
 SHAH, A. M., SMAS, M. E., KORIR, G. K., FLOYD, F. P., GILMAN, A. J., LORD, J. B., WINOKUR, D.,
 SPRINGER, S., IRIMIA, D., NAGRATH, S., SEQUIST, L. V., LEE, R. J., ISSELBACHER, K. J., MAHESWARAN,
 S., HABER, D. A. & Toner, M. 2010 Isolation of circulating tumor cells using a microvortexgenerating herringbone-chip. *Proc. Natl. Acad. Sci. U.S.A.* 107 (43), 18392–18397.
 - generating herringbone-chip. *Proc. Natl. Acad. Sci. U.S.A.* **107** (43), 18392–18397. Stroock, Abraham D, Dertinger, Stephan K, Whitesides, George M & Ajdari, Armand 2002*a*

- Patterning flows using grooved surfaces. *Anal. Chem.* **74** (20), 5306–5312.

 Stroock, A. D., Dertinger, S. K. W., Ajdari, A, Mezić, I., Stone, H. A. & Whitesides, G. M. 2002*b*Chaotic mixer for microchannels. *Science* **295** (5555), 647–651.
- 583 Stroock, Abraham D & McGraw, Gregory J 2004 Investigation of the staggered herringbone mixer with a simple analytical model. *Philos. Trans. R. Soc. A* **362** (1818), 971–986.
- THIELICKE, WILLIAM & SONNTAG, RENÉ 2021 Particle image velocimetry for matlab: Accuracy and enhanced algorithms in pivlab. *Journal of Open Research Software* **9** (1).
- USPAL, W. E., ERAL, H. B. & DOYLE, P. S. 2013 Engineering particle trajectories in microfluidic flows using particle shape. *Nat. Commun.* **4** (1), 1–9.
- 589 Whitesides, G. M. 2006 The origins and the future of microfluidics. *Nature* **442** (7101), 368–373.